Full Length Article

Effect of calcium dispersion and graphitization during high-temperature pyrolysis of beech wood char on the gasification rate with CO_2

Christoph Schneider[a,*], Stella Walker[a], Aekjuthon Phounglamcheik[b], Kentaro Umeki[b], Thomas Kolb[a,c]

[a] Karlsruhe Institute of Technology, Engler-Bunte-Institute, Fuel Technology, EBI ceb, Engler-Bunte-Ring 1, 76131 Karlsruhe, Germany
[b] Luleå University of Technology, Department of Engineering Sciences and Mathematics, Division of Energy Science, 97187 Luleå, Sweden
[c] Karlsruhe Institute of Technology, Institute for Technical Chemistry, ITC vgt, Hermann-von-Helmholtz-Platz 1, 76344 Eggenstein-Leopoldshafen, Germany

A B S T R A C T

This paper presents thermal deactivation of beech wood chars during secondary pyrolysis in a drop-tube reactor. Pyrolysis temperature was varied between 1000 °C and 1600 °C at a constant residence time of 200 ms. The effect of pyrolysis conditions on initial conversion rate R_0 during gasification, graphitization of the carbon matrix and ash morphology was investigated. Gasification experiments for the determination of R_0 were conducted in a thermogravimetric analyzer using pure CO_2 at 750 °C and isothermal conditions. A linear decrease in initial conversion rate R_0 was observed between 1000 °C and 1400 °C. However, a strong increase of R_0 at 1600 °C was encountered. Micropore surface area of the secondary chars showed no correlation with the initial conversion rate R_0 during gasification with CO_2. Graphitization of the carbon matrix was determined using X-ray diffraction and Raman spectroscopy suggesting the growth of aromatic clusters and graphite-like structures for increasing pyrolysis temperatures up to 1600 °C. Furthermore, CaO dispersion was analyzed quantitatively and qualitatively using temperature-programmed reaction at 300 °C as well as SEM/TEM. CaO dispersion D_{CaO} decreases steadily between 1000 °C and 1400 °C whereas a strong increase can be observed at 1600 °C, which is in good accordance with the development of the initial conversion rate R_0 as a function of pyrolysis temperature. SEM/TEM images indicate the formation of a thin CaO layer at 1600 °C that is presumably responsible for the strong increase in initial conversion rate R_0 at this temperature. When excluding the catalytic activity of CaO via formation of the ratio $R_0\,D_{CaO}{}^{-1}$, increasing graphitization degree has a linear negative influence on char reactivity at pyrolysis temperatures between 1000 °C and 1400 °C.

1. Introduction

The use of low-grade biogenic and fossil fuels in high-pressure entrained-flow gasification (EFG) allows for the production of high-quality synthesis gas, which can be converted into fuels and chemicals or used for power generation via integrated gasification combined cycle (IGCC) systems. In the near future, EFG will play an important role in satisfying the demand for basic chemicals and power [1,2]. In EFG, the fuel is converted via thermal and thermo-chemical processes i.e. drying and pyrolysis under high heating rates as well as the subsequent heterogeneous gasification reactions of the resulting char in a CO_2- and H_2O-rich atmosphere. For the achievement of high cold gas efficiencies, a complete char conversion is desired. Since the heterogeneous reactions are considered as the rate-limiting step for complete fuel conversion, the knowledge of the gasification kinetics is essential for the design of entrained-flow gasifiers [3].

2. Literature review

During the pyrolysis step in the flame zone of the entrained-flow gasifier, the char undergoes various changes concerning chemical and physical properties of both carbon matrix and inorganic ash components. In this context, high temperatures and long residence times typically lead to a loss of reactivity in the subsequent gasification process. This effect is called thermal deactivation or "thermal annealing" and can be the consequence of thermal stress during pyrolysis and gasification of fossil [4–9] or biomass-based solid fuels [10–12].

One reason for the loss of reactivity is the graphitization of the carbon matrix. Graphitization describes the process of increase and arrangement of graphene layers in carbonaceous materials [6]. This process is characterized by formation, growth and order of aromatic clusters and graphite crystals [8,9,13]. In raw solid fuels such as coal or

biomass, most of the carbon is available as turbostratic. Turbostratic carbon consists of graphene layers, which are disordered and non-planar. If these layers are accompanied by other types of carbon bonds (e.g. sp^2- or sp^3-bonds) or even heteroatoms (e.g. H, O, N, S), the present structure is titled as amorphous carbon [13,14].

During pyrolysis of solid biogenic fuels, cracking reactions occur and lead to condensation, polymerization and the formation of aromatic carbon clusters [12,15]. Below pyrolysis temperatures of 500 °C, ordered and/or turbostratic carbon is very low while basic structures are present predominantly. Between 800 °C and 1500 °C, nanocrystalline graphite grows and associates face-to-face in distorted columns. From 1600 °C to 2000 °C, these columns coalesce into distorted wrinkled layers. These layers stiffen and become flat above 2100 °C [8,9,16–18]. Many authors have proven that graphitization progresses at higher residence times at high temperatures resulting in a char with low reactivity towards combustion and gasification [14,19–22]. This is due to the fact, that the number of carbon atoms in an amorphous structure, at defect sites or at the edge of a graphene layer decreases with increasing graphitization. Carbon atoms located in these areas are more reactive than those inside an aromatic cluster [9]. Common methods for the experimental determination of a graphitization degree can be found in literature using X-ray diffraction (XRD) [13,14,23,24] and Raman spectroscopy [17,18,23,25,26].

Another aspect affecting char reactivity is the influence of inorganic, ash-forming elements in the fuel [12,27–33]. Especially alkali [34–46] and alkaline earth metals [39–49] evoke an increase of char reactivity during gasification with CO_2 and H_2O. Struis et al. [44] investigated the catalytic activity of major metal species (Na, K, Ca, Mg, Zn, Pb, Cu) found with waste wood during the gasification of nitrate salt impregnated charcoal with CO_2. Results indicated a superposition of structural changes in the charcoal micropore domain and catalyst-specific effects during gasification of the impregnated char samples. Gasification of the samples impregnated with alkali nitrate salts resulted in a reaction rate maximum at a carbon conversion degree of $X_C = 0.5 – 0.7$. The authors explained this maximum with an accumulation of an oxidic alkali type catalyst (M_xO_y) being formed during the early gasification stage. Furthermore, alkaline earth nitrate salts exhibited a high catalytic activity during the early gasification stage. However, a decreasing reaction rate for the whole carbon conversion range was observed, likely due to sintering of the resulting alkaline earth metal oxide, as the authors presumed. In contrast, silicon and phosphorous may inhibit the gasification reaction by binding catalytically active compounds such as potassium [34,35,50].

An important parameter to evaluate the catalytic activity of ash forming elements is the dispersion on the char surface [31,51]. Cazorla-Amoros et al. [52] investigated the dispersion and sintering of Ca species on carbon samples during pyrolysis and gasification with CO_2. They found a strong link between Ca dispersion and carbon-CO_2 reactivity and were able to deduce the following findings: first, a high heating rate during pyrolysis resulted in a high calcium dispersion. Second, Ca dispersion decreased with increasing carbon burn-off during gasification with CO_2 suggesting a deactivation mechanism presumably due to sintering processes. Furthermore, results showed the enormous effect of chemical state of calcium ($CaCO_3$ or CaO) on the sintering rate. It was observed that $CaCO_3$ had a much higher mobility on the carbon surface than CaO because of the great difference in their Tammann temperatures (see Eq. (2)).

The dispersion is normally used for the characterization of a catalyst in order to either determine the number of catalyst particles on a support material or the number of active sites in relation to the carrier mass or available surface area [53]. Depending on the experimental method, various definitions for the catalyst dispersion may be appropriate. Established methods for the determination of dispersion are e.g. chemisorption, XRD as well as scanning (SEM) and transmission (TEM) electron microscopes [51,53–56]. If chemisorption is used for the determination of dispersion, it is convenient to define the dispersion as

the number of active sites (species B) per mass or specific surface area of the carrier material (species A) in $mol_B\ g_A^{-1}$ or $mol_B\ m_A^{-2}$ [57,58].

In the frame of the present work, catalytic activity of ash forming elements is discussed based on an analogy with synthesized catalysts. Deactivation of synthesized catalysts may occur due to poisoning of active sites or a decrease in the catalytically active surface area hence a lower dispersion of catalytically active particles. If this lower dispersion is thermally driven, the decrease in catalytically active surface area can be attributed to sintering processes [51,53]. For sintering processes and particle migration, three temperatures are relevant: melting temperature T_{melt}, Hüttig temperature $T_{Hü}$ and Tammann temperature T_{Ta}. Detachment and migration of metal atoms are enabled starting at Hüttig temperature $T_{Hü}$. Reaching Tammann temperature T_{Ta}, entire particle migration over the support surface, accompanied by particle collision and coalescence may occur [51,59]. Following estimations for these two temperatures can be found in the literature [51,52]:

$$T_{Hü} = 0.3 T_{melt} \tag{1}$$

$$T_{Ta} = 0.5 T_{melt} \tag{2}$$

Recent studies concerning thermal deactivation of biomass chars during pyrolysis mainly focus on the change of carbonaceous structures. Guizani et al. [60] investigated the influence of entrained flow pyrolysis conditions on biomass char properties. Temperatures of 500 °C–1400 °C were applied. Morphology of the resulting chars was highly modified at high temperature with loss of the initial wood cell structure, sintering and macropore formation. Char reactivity determined by oxidation with O_2 decreased significantly with increasing pyrolysis temperature. Furthermore, Raman analyses showed that the carbonaceous structures ordered with increasing temperature. The authors developed several correlations between char reactivity and the oxygen-to-carbon-ratio as well as parameters deduced from Raman spectroscopy i.e. total Raman area and intensity ratio I_V/I_D. In 2019, Guizani et al. [25] developed the heat treatment severity index (HTSI) taking into account reactor temperature and residence time of a biomass particle during pyrolysis under entrained-flow conditions. Again, several correlations between the HTSI and physicochemical char properties were formed. Senneca et al. [26] investigated coal and biomass pyrolysis in N_2 and CO_2 atmosphere. They reported a remarkable degree of structural order being developed by the biomass chars upon severe heat treatment. This structural order was determined by Raman spectroscopy.

Other authors also couple the change in ash composition, formation and sintering of ash particles to thermal deactivation processes of biomass chars during pyrolysis. Trubetskaya et al. [24] pyrolyzed wheat straw and rice husk in an entrained-flow reactor at high temperatures and heating rates and investigated the effect of inorganic matter on char morphology. They reported that the silicon compounds were dispersed throughout the turbostratic structure of rice husk char in an amorphous phase with a low melting temperature leading to the formation of a glassy shell covering the carbonaceous char matrix and preserving the char particle shape and size. However, the effect of the silicon oxides on char reactivity with respect to oxidation in O_2 was less pronounced. Strandberg et al. [61] found that during pyrolysis of wheat straw, which is rich in Si and K, a molten ash layer is encapsulating the char. During the subsequent gasification process, this ash layer inhibits the gasification reaction and forms a diffusion barrier preventing carbon oxidation.

The objective of this study is to investigate the thermal deactivation of beech wood char during pyrolysis in a drop-tube reactor under high heating rates. The vast majority of previous research work focuses on the increasing graphitization during pyrolysis of solid fuels in order to explain thermal deactivation of the char produced. Only few publications investigate the dispersion of catalytically active ash components of chars at very high pyrolysis temperatures and its influence on the subsequent gasification reaction. This work aims to estimate the influence of both graphitization and inorganic dispersion on thermal

deactivation. Especially, it presents the dispersion of calcium species on the biomass char surface for pyrolysis temperatures up to 1600 °C where literature data is very limited. Thermal deactivation was quantified by gasification experiments with CO_2 in a thermogravimetric analyzer. Furthermore, graphitization was determined using XRD and Raman spectroscopy while inorganic dispersion was investigated using chemisorption, SEM and TEM.

3. Materials and methods

3.1. Fuel

Commercially available primary char (Holzkohleverarbeitung Schütte GmbH & Co. KG) was purchased and used as precursor since the same char is utilized in the bioliq ® EFG for research operation. It is produced under mild conditions at an estimated pyrolysis temperature of 500 °C to 600 °C. Table 1 shows the proximate and ultimate analysis of the primary char. It still contains approx. 12 wt% of volatiles and consists of 1.8 wt% ash and 85.5 wt% fixed carbon. Furthermore, the organic components consist of approx. 90 wt% carbon, 3 wt% hydrogen and 7 wt% oxygen (by difference). For secondary pyrolysis in the drop-tube reactor, the primary char was sieved to a particle fraction of 50–150 μm.

3.2. Drop-tube reactor

The drop-tube reactor (DTR) consists of an oven (HTM Reetz GmbH) with three heating zones (l_{H1} = 200 mm, l_{H2} = 917 mm, l_{H3} = 200 mm) and a total length of 2000 mm. Each heating zone can be heated to a maximum temperature of 1700 °C. An alumina oxide reaction tube (Aliaxis Deutschland GmbH) with a length of 2100 mm and the inner diameter of 20 mm is inserted vertically in the oven. The temperature calibration was conducted with a type B thermocouple, which was introduced into the reactor from the top under steady-state gas flow. Gas temperature profiles for the pyrolysis experiments can be found in the supplementary material section. A coaxial alumina oxide pipe (length 810 mm, inner diameter 4 mm) was used to feed argon (tracer and carrier gas) and the primary char into the reactor. The feeding system consists of a slowly rotating ceramic disc (Pure Feed DP-4, Schenck Process Europe GmbH) enabling stable solid mass flow rates of approx. 1 g min^{-1}. The primary char was mixed with the reaction gas at the beginning of the second heating zone. For the experiments presented in this work, gas velocity in the reactor was adjusted in order to ensure a gas-phase residence time in the isothermal zone of 200 ms using N_2 as core flow. N_2 volume flow was varied between 11.85 l min^{-1} and 17.44 l min^{-1} while Ar flow was varied between 0.52 l min^{-1} and 0.76 l min^{-1} leading to an N_2/Ar ratio of approx. 23. Ar flow was adjusted in order to ensure similar gas velocities inside the dosing and the reactor tube. At the outlet of the reactor, the hot reaction gas and secondary char were cooled by an inert gas quench to temperatures below 400 °C. Subsequently, the char samples were separated in a hot gas cyclone and collected in a nitrogen-flushed lock for further analyses. The reactor pressure was controlled by two electrically controlled valves and set to 5 mbar gauge. Product gas was continuously monitored with infrared photometry (URAS, ABB) and micro gas chromatography (490 Micro GC, Agilent Technologies). Further information concerning the drop-tube reactor and the operating conditions can be found in literature [62,63]. Before each pyrolysis experiment, the primary char was dried for at least 12 h at 105 °C. In order to remove oxygen from the char surface, the fuel was set under vacuum and flushed with nitrogen five times. For secondary pyrolysis experiments, temperatures in the isothermal zone of the reactor were varied between 1000 °C and 1600 °C. All experiments and analyses were carried out at Engler-Bunte-Institute (EBI ceb), Karlsruhe Institute of Technology (KIT) if not denoted specifically.

3.3. Chemical analyses

Proximate analysis for the determination of moisture, volatiles and ash was conducted in accordance with DIN 51718, DIN 51719 and DIN 51720. Ultimate analysis for the determination of C/H/N/S was carried out in a vario Macro Cube (elementar) according to DIN 15104. Elemental composition of ash was analyzed by inductively coupled plasma optical emission spectrometry (ICP-OES) at the Institute for Applied Materials - Applied Materials Physics (IAM-AWP, KIT). Prior to ICP-OES, the char samples were incinerated at 815 °C followed by acid pressure digestion in a DAB-2 pressure vessel (Berghof) using a mixture of HNO_3, HCl and HF at 350 °C for 12 h. The hydrofluoric acid is later complexed with H_3BO_3 at 180 °C for 2 h.

3.4. Determination of initial conversion rate R_0

Determination of initial conversion rate R_0 of the char samples with CO_2 was carried out in a thermogravimetric analyzer (pTGA, Rubotherm GmbH). The pTGA consists of a magnetic suspension balance that allows for continuous recording of the sample mass with an accuracy of ± 10 μg. In the gasification experiments, a total gas flow of 100 ml min^{-1} was set. A sample mass of approx. 2 ± 0.1 mg was placed in a ceramic crucible (inner diameter 16 mm, height of wall 10 mm). After evacuating the pressure vessel to ensure an oxygen-free atmosphere, the reaction chamber was purged with argon. The fuel samples were heated up at a constant heating rate of 20 °C min^{-1} to the reaction temperature of 750 °C followed by 20 min holding time to ensure stable conditions. The samples were then gasified in 100% CO_2 at atmospheric pressure until the complete conversion of the fuel was reached.

Char conversion $X(t)$ was determined using the discrete mass signals $m(t)$, the initial mass m_0 and the remaining mass of ash m_{ash}:

$$X(t) = \frac{m_0 - m(t)}{m_0 - m_{ash}} \tag{3}$$

$$R_m = -\frac{1}{m(t) - m_{ash}}\frac{dm}{dt} = \frac{1}{1 - X(t)}\frac{dX}{dt} \tag{4}$$

R_m is the specific conversion rate and can be calculated as presented in Eq. (4). Furthermore, R_X is defined as the conversion rate described by a rate coefficient $R(T,p)$ and a structural term $F(X)$:

$$R_X = \frac{dX}{dt} = R(T, p)F(X) \tag{5}$$

In the frame of this work, the Uniform Conversion Model (UCM) was used to model the char conversion process resulting in a structural term of $F(X) = 1 - X$. Thus, the following expression is obtained:

$$R_X = \frac{dX}{dt} = R_0(1 - X) \tag{6}$$

$$R_0 = \frac{dX}{dt}\bigg|_{X=0} \tag{7}$$

R_0 is defined as the initial conversion rate, which was determined by

Table 1
Properties of primary char.

Proximate analysis/wt%, ad	
Moisture	0.9
Ash content	1.8
Volatiles	11.8
Fixed carbon	85.5
Ultimate analysis/wt%, daf	
C	89.8
H	2.6
O (diff)	7.2
N	0.4

a least-square fit in the char conversion range between 20% and 50%. This range was chosen in order to minimize the effects of gas exchange in the pTGA at the start of each experiment. Furthermore, the char properties for higher conversion degrees may have changed and were not characterized anymore. Gasification experiments were repeated three times.

3.5. Micropore surface area

Micropore surface area of the char samples was determined in a physisorption analyzer (ASAP 2020, Micromeritics) using CO_2 at 0 °C. For each adsorption experiment, relative pressure ranges from $1 \cdot 10^{-5}$ to 0.035 were applied. Prior to adsorption, the char samples were heated to 180 °C for 12 h. Data evaluation was carried out based on the Dubinin-Radushkevich method (DR) for micropores in activated carbon.

3.6. Graphitization

X-ray diffraction (XRD) was carried out at Luleå University of Technology using an Empyrean (Malvern Panalytical) diffractometer. Char samples were placed in an alumina sample holder and analyzed in a range of $10° \leq 2\theta \leq 90°$, a step size of 0.0065652° and a step duration time of 99.45 s. The chosen step size enables the detection of graphite, carbon nanocrystals and amorphous carbon. Furthermore, inorganic species like crystalline calcium carbonate were visible. Cu Kα radiation (λ = 1.542 Å) was used as an X-ray source.

XRD analysis was conducted using the full-width at half maximum (FWHM) of the characteristic carbon peaks at approx. $2\theta = 24°$ and $2\theta = 44°$. The first maximum (23° − 24°) can be attributed to the (0 0 2)-Peak, the second (44°) to the (1 0 0)-Peak. The (0 0 2)-Peak represents the reflection at stacked graphene layers whereas the (1 0 0)-Peak originates from reflection at aromatic ring structures within the graphene layers. Furthermore, narrow peaks represent crystalline structures [19,64,65].

Scherrer equation (Eq. (8)) allows for the quantification of graphitization in terms of growth of nanosized carbon crystals:

$$L_i = \frac{K_i \lambda}{B_i \cos(\theta_i)} \quad i = a, c \tag{8}$$

Here, L_i stands for calculated sizes of the nanosized carbon crystals and can be determined using the ratio of X-ray wavelength λ and a structural constant K_i divided by the value for FWHM B_i and the cosine of the reflection angle θ_i. The indices a and c indicate two different sizes of the nanosized carbon crystals: L_a describes the radial expansion of the carbon crystal ((1 0 0)-Peak) while L_c stands for the stacking height of the graphene layers ((0 0 2)-Peak). Values for the structural constants $K_a = 1.84$ and $K_c = 0.89$ are taken from literature [14,20,22,23,64,65]. As a measure for increasing graphitization, the ratio $L_a L_{a,0}^{-1}$ was formed. Here, $L_{a,0}$ describes the radial expansion of nanosized carbon crystals of the primary char.

The distance between two graphene layers d is calculated using Bragg equation for $n = 1$:

$$2d\sin(\theta_c) = n\lambda \tag{9}$$

Raman spectroscopy was carried out at Luleå University of Technology using a Senterra II (Bruker) microscope. 30 measurements (co-additions) at 3 s were conducted per char particle with green laser (λ_{Laser} = 532 nm) and low power of 0.2 mW in order to minimize structural changes in the carbon matrix. Three different particles per char sample were analyzed using this approach. During Raman measurements, two intensity maxima were encountered at Raman shifts of approx. 1355 cm^{-1} and 1575 cm^{-1} representing the D- and the G-Peak, respectively. While the G-Peak originates from the vibration within aromatic clusters of nanosized carbon crystals, the D-Peak can be attributed to defects in the graphite crystal or boundary areas of graphene layers [17,18,66]. Furthermore, a valley peak (V-Peak) is located between D- and G-Peak, which can be traced back to amorphous, sp^2-hybridized carbon [13,26,67]. The evaluation of Raman spectra was carried out using the intensity ratios of D- and G-Peak (I_D/I_G) as well as V-and D-Peak (I_V/I_D). Beforehand, the intensities were normalized to the maximum intensity of the G-Peak.

3.7. Ash dispersion

Quantification of ash dispersion was carried out in the pTGA (see chapter 3.4) using temperature-programmed reaction (TPR). In the frame of this work, ash dispersion is determined by chemisorption of CO_2 on CaO at 300 °C, as the element Ca is most abundant in the ash of the char samples and known to catalyze the gasification reaction (see chapter 2). At 300 °C, CO_2 reacts with CaO atoms at the surface of ash particles forming $CaCO_3$. Increasing the temperature would lead to a carbonization of bulk CaO due to diffusion of CO_2 into the ash particle [58]. Thus, chemisorption of CO_2 at 300 °C can be used to determine the outer surface of CaO particles in the biomass ash giving a value for the dispersion of CaO particles. This approach is based on the assumption that no other compound in the ash interacts with CO_2 at this temperature.

In each TPR experiment, 30 ± 0.1 mg of char sample and a CO_2 volume flow of 100 ml min^{-1} was used. Prior to the chemisorption segment, the pTGA was evacuated and backfilled with Argon. Subsequently, the sample was heated to 850 °C in order desorb gases and decompose any $CaCO_3$ if present. Melting, Hüttig and Tamman temperature of CaO are shown in Table 2. In the following segment, the sample was cooled to 300 °C and stabilized in Argon. Chemisorption started switching the gas atmosphere from pure Argon to a mixture of 90 vol-% Ar and 10 vol-% CO_2 and lasted for 300 min.

The chemisorbed mass of CO_2 was calculated as difference between the mass signals after and before the chemisorption segment (average values of the last 30 mass signals of stabilizing segment m_{Stab} and chemisorption segment m_{Chem}, Eq. (10)). Assuming an equimolar stoichiometry for the reaction of surface CaO with CO_2, the molar amount of surface CaO can be directly calculated (Eq. (11)). The dispersion D_{CaO} of surface CaO is then based on the weighed out amount of char m_{Char} in $mol_{surface-CaO} g_{char}^{-1}$ (Eq. (12)).

$$m_{CO_2} = m_{Chem} - m_{Stab} \tag{10}$$

$$n_{CO_2} = \frac{m_{CO_2}}{M_{CO_2}} = n_{CaO} \tag{11}$$

$$D_{CaO} = \frac{n_{CaO}}{m_{char}} \tag{12}$$

Scanning electron microscope (SEM) images were taken at Laboratory for Electron Microscopy (LEM, KIT) using a LEO 1530 (Zeiss) with an accelerating voltage of $U = 5$ keV. Prior to SEM analysis, the char sample was positioned on a conductive adhesive tape and coated with a 5 nm layer of platinum (Leica EM ACE600). Four different magnifications (400x, 4000x, 20 000x and 100 000x) were used for each char sample.

Transmission electron microscopy (TEM) was also conducted at LEM (KIT) using a FEI Osiris ChemiSTEM microscope coupled with Quantax system (Bruker) as energy dispersive X-ray (EDX) detector and an accelerating voltage of $U = 200$ keV. The char samples were

Table 2
Melting, Hüttig and Tammann temperature of CaO.

Material	T_{melt} °C	$T_{Hü}$ °C	T_{Ta} °C
CaO	2613 [68]	784	1307
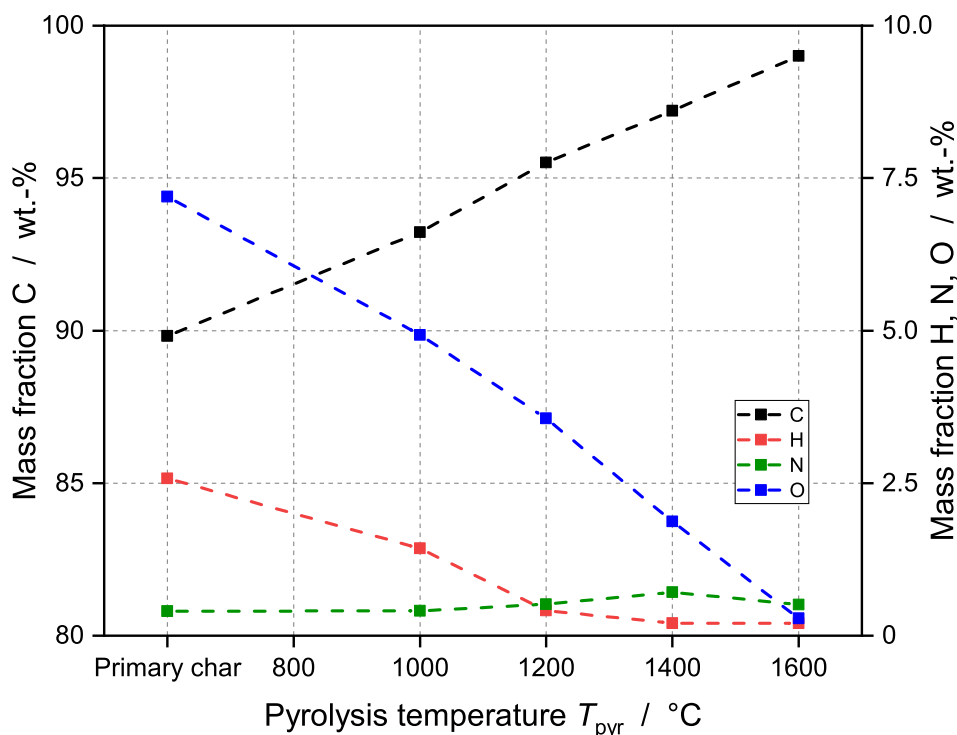
Fig. 1. Chemical composition of primary and secondary chars as a function of pyrolysis temperature. Secondary pyrolysis was carried out in a DTR applying N_2 atmosphere and 200 ms residence time.

dispersed in ethanol and the droplets placed on copper wire with a mesh size of 400 μm.

4. Results and discussion

4.1. Chemical analyses

Fig. 1 shows the chemical composition of primary and secondary chars as a function of pyrolysis temperature. The primary char contains approx. 90 wt% carbon. A steady increase of carbon from 90 wt% to 99 wt% and steady decrease of oxygen from 7.2 wt% to almost zero at 1600 °C can be observed. At 1600 °C, the char consists almost of pure carbon. Nitrogen remains constant at a low level while hydrogen decreases from 2.5 wt% to approx. 0 wt% at 1200 °C.

Table 3 shows the ash elemental analysis of primary and secondary chars determined using ICP-OES. As can be seen from the table, the main ash component of this beech wood char is calcium. The calcium content remains almost constant at approx. 39 wt% with increasing pyrolysis temperature. A slight decrease of approx. 4 wt% at 1400 °C can be observed. Potassium halves at 1000 °C and 1200 °C and increases to approx. 5 wt% at 1400 °C and 1600 °C. Magnesium decreases from 1400 °C being only 1 wt% at 1600 °C. Silicon is between 2 and 3 wt% while phosphorous remains almost constant during secondary pyrolysis

(P content of primary char was not determined). K/Si ratios range from 0.83 to 2.30 while K/(Si + P) ratios range from 0.51 to 1.29 being very low in total (not shown in table 3). Thus, deactivation of K by Si and P can be assumed [34,69].

4.2. Determination of initial conversion rate R_0

Gasification experiments of the char samples with CO_2 at 750 °C in a pTGA are discussed in this chapter. Fig. 2 shows the conversion curves during gasification for the primary beech wood char as well as the secondary chars with different pyrolysis history. As can be seen from Fig. 2 A, the primary char was completely gasified within 100 min. Samples pyrolyzed at 1000 °C and 1600 °C were gasified after approx. 150 min (see Fig. 2 B & D). The longest conversion time with approx. 200 min is observed for the sample pyrolyzed at 1400 °C (see Fig. 2 C). The different pyrolysis conditions also affect the shape of the conversion curves (see Fig. 2, orange curves are approximated with 6th-degree polynomial method except Fig. 2 C). In particular, the different shapes of the conversion curves become striking for the sample P1400C_200ms. Here, a constant conversion rate between 20% and 80% conversion degree can be observed. Therefore, the conversion rate $\frac{dX}{dt}$ was set constant in order to make the calculated initial conversion rate R_0 comparable to the other samples.

Table 3
Ash elemental analysis of primary and secondary chars.

Element	Primary char	P1000C_200ms	P1200C_200ms	P1400C_200ms	P1600C_200ms
wt%					
Ca	38.20	39.00	39.50	35.30	39.10
K	4.62	2.54	2.61	5.48	5.05
Mg	6.03	7.13	7.08	5.8	1.03
Si	2.01	3.05	2.97	2.51	2.45
P	n. a.	1.95	1.99	1.73	1.52
Na	0.82	0.76	0.76	0.96	0.84
Fe	0.74	1.05	0.82	0.84	0.83
Al	0.25	0.34	0.29	0.28	0.31
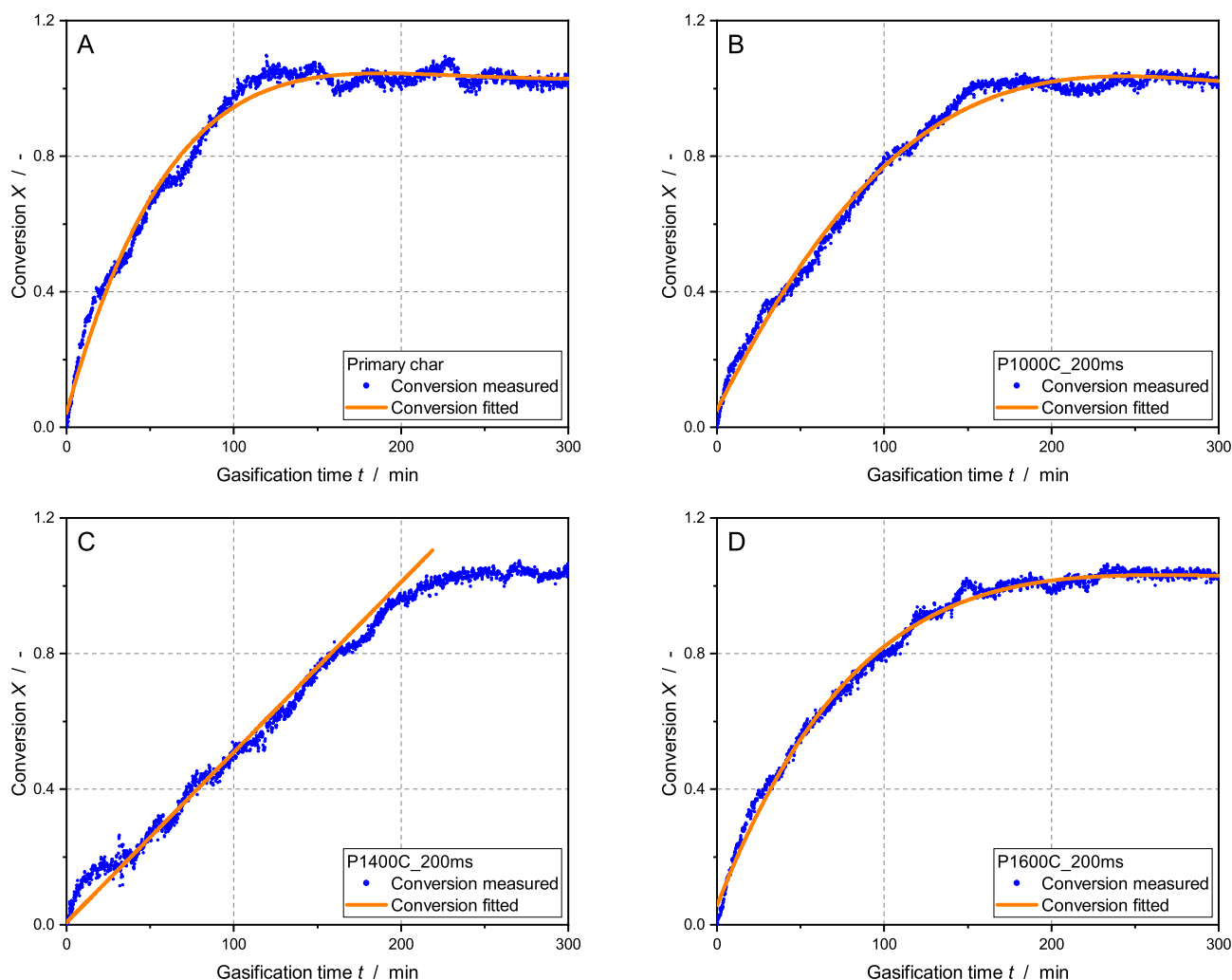
Fig. 2. Measured and fitted conversion curves during gasification in CO_2 for beech wood chars with different secondary pyrolysis history (pTGA, 750 °C, atmospheric pressure, 100% CO_2).

From the fitted conversion curves in Fig. 2 (orange), the conversion rates $\frac{dX}{dt}$ were calculated (see Fig. 3). As stated above, the conversion rate of P1400C_200ms is set to be constant in the conversion range considered. All other samples show a decreasing conversion rate for higher conversion degrees which may be an indication of a calcium catalyzed gasification reaction [44,70].

Fig. 4 shows the initial conversion rate R_0 during gasification of different beech wood chars with CO_2 as a function of pyrolysis temperature. The primary char has the highest initial conversion rate R_0 among the chars investigated. Due to thermal deactivation during secondary pyrolysis, the initial conversion rates decrease between 1000 °C and 1400 °C almost linearly. However, a strong increase in the initial conversion rate at 1600 °C is observed that cannot be explained by thermal deactivation due to graphitization of the carbon matrix. Thus, other effects also influence the initial conversation rate of gasification with CO_2.

4.3. Micropore surface area

Micropore surface area determined via physisorption of CO_2 at 0 °C using Dubinin-Radushkevich is depicted in Fig. 5. The primary char shows a micropore surface area of approx. 395 m^2 g^{-1}. A slight increase at pyrolysis temperatures of 1000 °C and 1200 °C is observed. Due to devolatilization at high heating rates during pyrolysis, micropore surface area is generated additionally. Increasing the pyrolysis
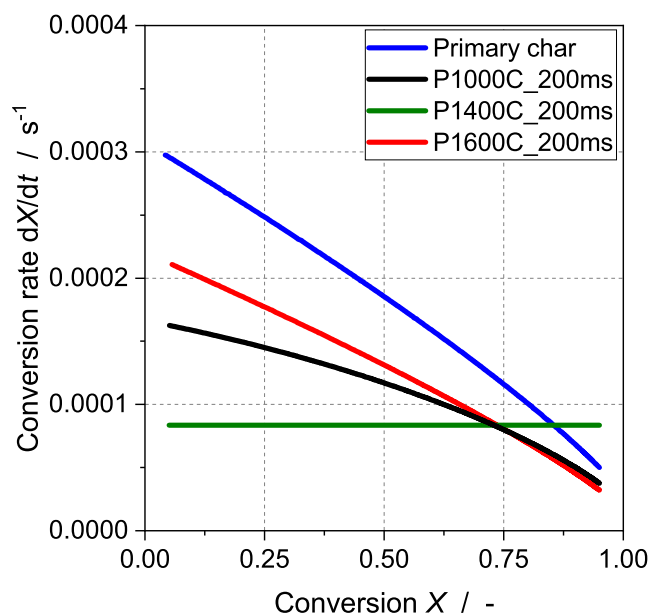
Fig. 3. Calculated conversion rates during gasification of different beech wood chars with CO_2 in pTGA (750 °C, atmospheric pressure, 100% CO_2).
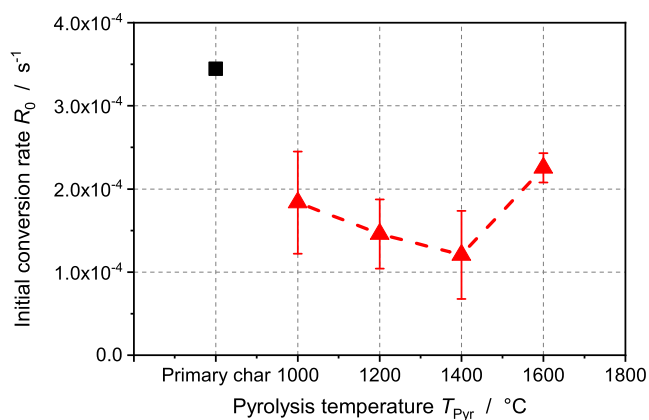
Fig. 4. Initial conversion rate R_0 during gasification of different beech wood chars with CO_2 in pTGA (750 °C, atmospheric pressure, 100% CO_2) as a function pyrolysis temperature.
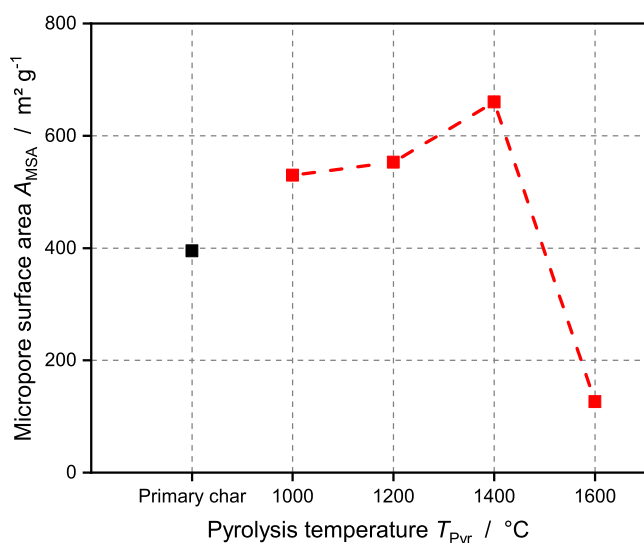
Fig. 5. Micropore surface area via physisorption of CO_2 at 0 °C using Dubinin-Radushkevich as a function of pyrolysis temperature.

temperature leads to an even higher micropore surface area at 1400 °C which may be attributed not only to devolatilization especially at high heating rates but also secondary reactions of the pyrolysis products with the char i.e. Boudouard reaction of released CO_2 with carbon forming carbon monoxide. This hypothesis was further supported by complementary gas-phase measurements showing no CO_2 in the off-gas starting at pyrolysis temperatures of 1400 °C and higher. At 1600 °C, micropore surface area collapses to approx. 126 $m^2\,g^{-1}$ which may be explained by ash fusion since melting of mineral matter could change the micropore structure and lead to a blocking of micropores [71,72]. This hypothesis is also supported by SEM/TEM images that show the formation of a thin ash layer on the char surface at 1600 °C (see chapter 4.5). Furthermore, no correlation between initial conversion rate and evolution of micropore surface area can be deduced.

4.4. Graphitization

XRD spectra of primary and secondary chars are depicted in Fig. 6. The intensity maxima for all samples are encountered at reflection angles 2θ of 23°–24° and 44°. The first maximum (23°–24°) can be attributed to the (0 0 2)-Peak, the second (44°) to the (1 0 0)-Peak (see chapter 3.6). The (0 0 2)-Peak represents the reflection from stacked graphene layers whereas the (1 0 0)-Peak originates from reflection from aromatic ring structures

within the graphene layers. Furthermore, narrow peaks represent highly crystalline structures [19,20,22,23,64,65]. Both peaks grow with increasing pyrolysis temperature. In particular, the (1 0 0)-Peak becomes more prominent for the secondary chars compared to primary char. Thus, the radial growth of graphene layers with increasing pyrolysis temperature is shown. From the evolution of the (0 0 2)-Peak, it can be concluded that the primary char already contains structured carbon to a certain degree. However, the amount of nanocrystals consisting of aromatic ring structures increases with increasing pyrolysis temperature. Another narrow peak can be observed for the primary char at approx. 29°. This peak is characteristic for crystalline calcium carbonate that is still present in the primary char [23]. During secondary pyrolysis, which is carried out above the decomposition temperature of calcium carbonate (700 – 825 °C), the calcium carbonate is decomposed.

Quantitative evaluation of the (0 0 2)- and (1 0 0)-Peak is carried out using Bragg's Law ($n = 1$) and Scherrer-Equation in order to calculate the mean distance between graphene layers d, stacking height L_c and radial expansion L_a (see chapter 3.6). Radial expansion L_a increases significantly with increasing pyrolysis temperature while distance d and stacking height L_c remain almost constant (see Fig. 7). By forming the ratio of L_c and d, the number of graphene planes per stack unit can be calculated. The stack units consist of 4 planes, each plane with a distance of $d = 3.87 \pm 0,03$ Å apart. This value is – as expected – higher than the plane distance for pure graphite ($d_{graphite} = 3.354$ Å) [73]. Pure graphite is obtained at temperatures higher than 2100 °C [8,9].

To sum up the results of XRD analysis, the radii of parallel arranged aromatic ring structures increase with increasing secondary pyrolysis temperature. Furthermore, the order of stacks and stack height were found to be constant. An increase of both order of stacks and stack height would only be expected for temperatures higher than 1600 °C [9].

Raman spectroscopy results are depicted in Fig. 8 and complementary to XRD findings as they indicate the existence of aromatic clusters. All spectra show peaks at 1355 cm^{-1} (D-Peak) and 1575 cm^{-1} (G-Peak). The intensity of the D-Peak of secondary chars increases with increasing pyrolysis temperature indicating the growth of aromatic clusters and graphite crystals [17,66]. Moreover, the D-Peak of the primary char consists of two shoulders. The first shoulder at approx. 1200 cm^{-1} originates from non-crystallite, sp^3-hybridized carbon structures. The shape of the D-Peak becomes narrower with increasing pyrolysis temperature. The narrowing suggests a growing order of the carbon matrix during pyrolysis since non-crystallite carbon is released as volatiles or condensates/polymerizes into larger molecules such as aromatic clusters [12,74]. Ratios of intensity maxima I_D/I_G and I_V/I_D are shown in Fig. 9 as a function of pyrolysis temperature. Again, an increase in D-Peak intensity can be observed compared to the G-Peak and the Valley for temperatures up to 1400 °C. Furthermore, a stagnation of both ratios between 1400 °C and 1600 °C can be seen.

In summary, Raman spectra are complementary to the XRD results indicating the growth of aromatic clusters and graphite crystals in biomass char due to thermal stress during secondary pyrolysis.

4.5. Ash dispersion

Dispersion of CaO was determined by TPR with CO_2 in a pTGA at 300 °C (see chapter 3.7). TPR experiments of the primary char were not carried out since the method applied would have changed the char's initial ash morphology and composition. From XRD results, it is known that the primary char still contains crystalline $CaCO_3$, which would have been decomposed to CaO in the heating segment prior to TPR. Concerning the secondary chars, CaO dispersion decreases steadily from 1000 °C to 1400 °C (see Fig. 10), which is in accordance with the development of initial conversion rate as a function of pyrolysis temperature. The decrease may be explained by sintering of CaO particles upon heat treatment. The size distribution of ash nanoparticles is depicted in Fig. 14. A strong increase of CaO dispersion at 1600 °C
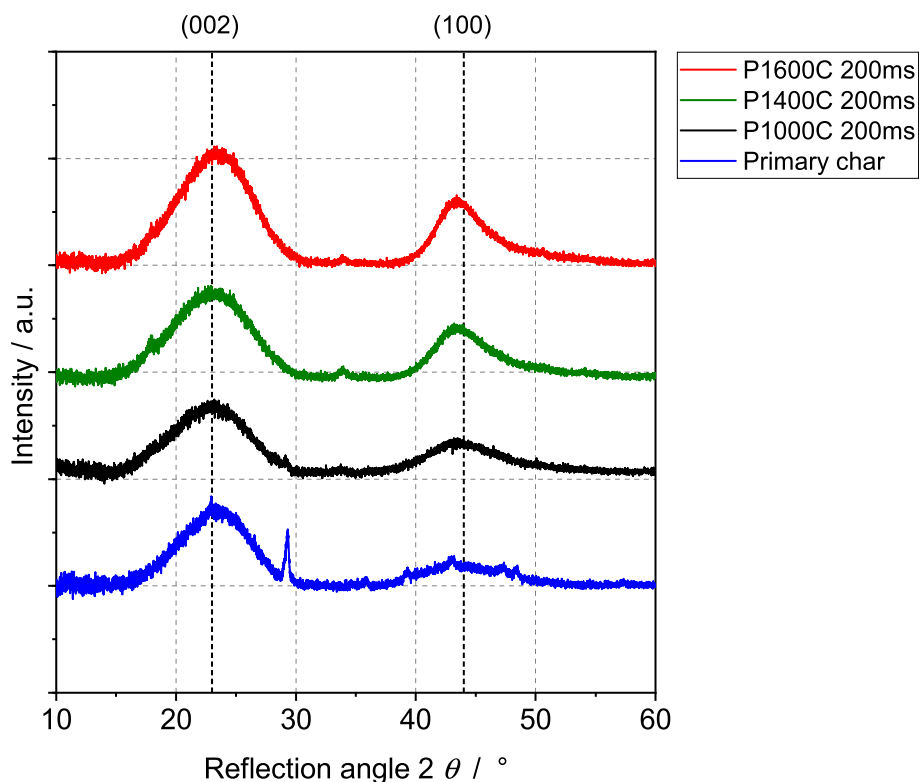
Fig. 6. XRD spectra of primary and secondary chars.
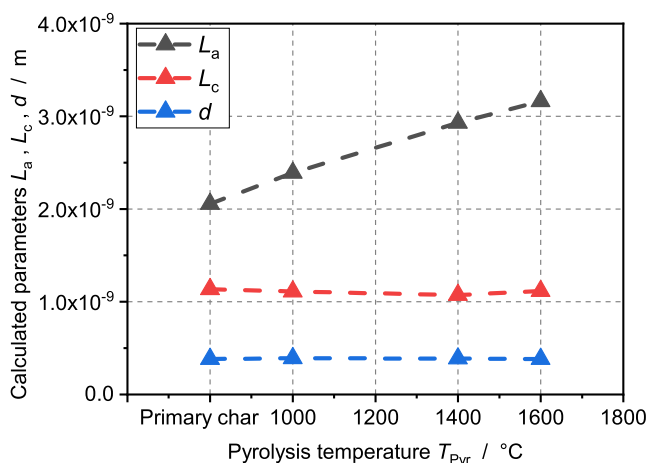
Fig. 7. Radial expansion L_a, stacking height L_c and distance between graphene layers d as a function of pyrolysis temperature.

correlating with increasing initial conversion rate at 1600 °C can be observed. This increase may be traced back to the formation of a thin CaO film on the char surface, which can be seen from SEM/TEM images in Figs. 11–13. The film connects catalytically active ash components to a multitude of carbon atoms on the char surface resulting in an increased initial conversion rate during gasification with CO_2 at 750 °C.

For qualitative evaluation of ash transformation upon heat treatment, SEM images with 20,000× and 100,000× magnification were taken. Fig. 11 shows SEM images of the primary and secondary chars with 20,000× magnification. The visible ash nanoparticles of primary char and P1000C_200ms are very similar. Larger particles are up to 1 μm and clearly distinguishable from the carbon underground. At 1400 °C, droplet-like nanoparticles have formed. However, the large ash particles of approx. 1 μm are still present. The transition between char surface and ash nanoparticles becomes more and more fluent with increasing temperature. For the sample P1600C_200ms, no distinction between char surface and ash nanoparticles can be made anymore suggesting the formation of a thin ash film on the carbon surface. Fig. 12 shows SEM images of two secondary char samples i.e. P1400C_200 ms and P1600C_200ms with 100,000× magnification. Ash nanoparticles of P1600C_200 ms are larger than those of P1400C_200ms. As can be seen from Fig. 14, sintering of ash nanoparticles occurs at higher temperatures. Furthermore, a droplet-like shape of ash particles becomes apparent for P1400C_200ms while for P1600C_200ms, a sharp boundary between carbon surface and ash particles cannot be drawn anymore. SEM images have shown that pyrolysis temperature has an immense impact on ash particle morphology and dispersion.

Complementary to SEM images, TEM analyses were carried out (see Fig. 13). TEM analyses were coupled with EDX in order to visualize the elements calcium (red) potassium (blue) and silicon (yellow) that are most abundant in the chars investigated. In Fig. 13, the TEM images of secondary char samples P1400C_200ms and P1600C_200ms are shown. Ca compounds undergo massive transformation due to heat treatment: On the one hand, sintering of nanoparticles takes place (see Fig. 14). On the other hand, Ca is again highly dispersed at a pyrolysis temperature of 1600 °C forming a catalytically active thin film on the carbon surface. Furthermore, all samples were found to have highly dispersed potassium and silicon compounds combined with oxygen irrespective of heat treatment. A fine dispersion of K and Si during pyrolysis supports
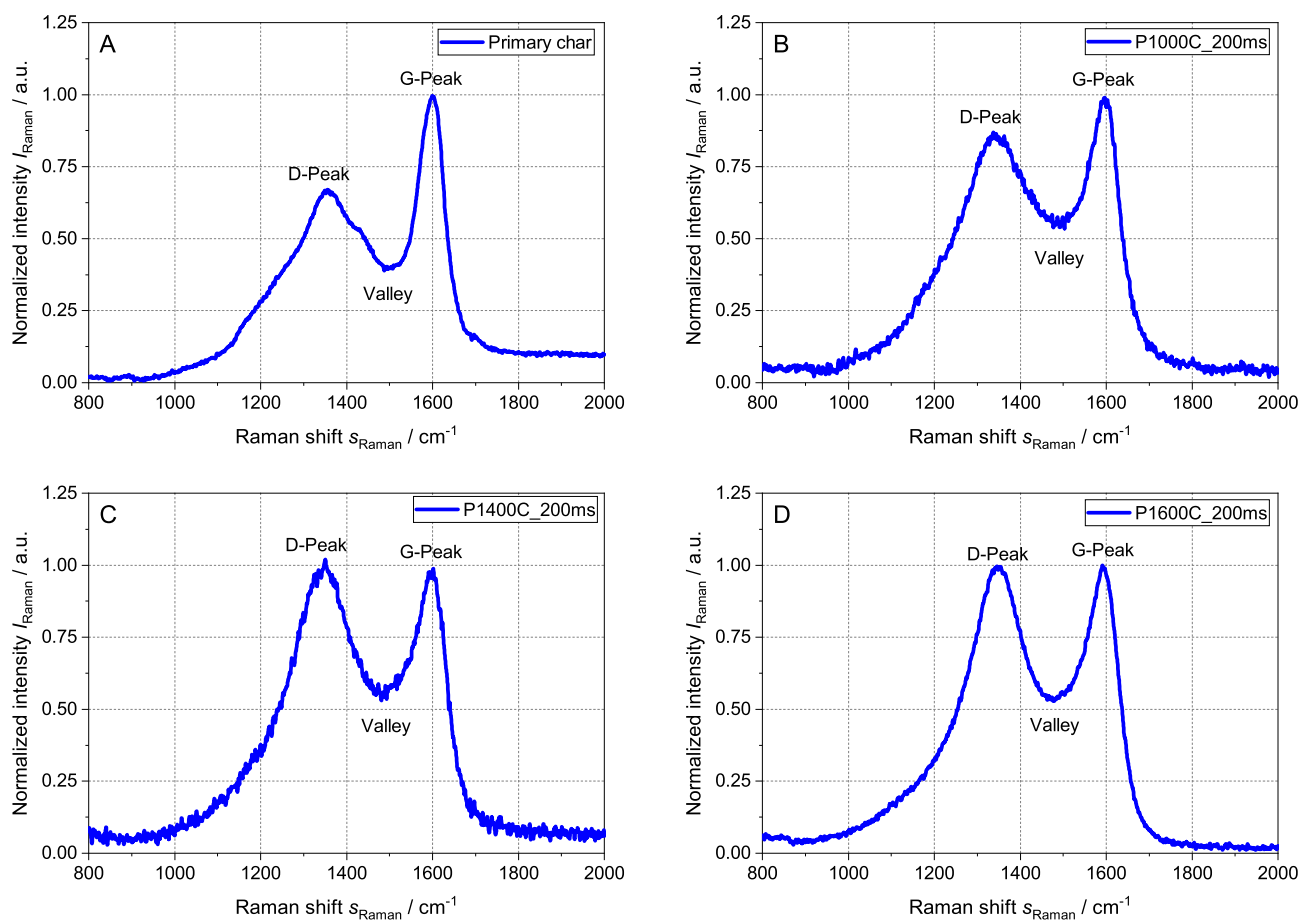
Fig. 8. Raman spectra of primary and secondary chars.
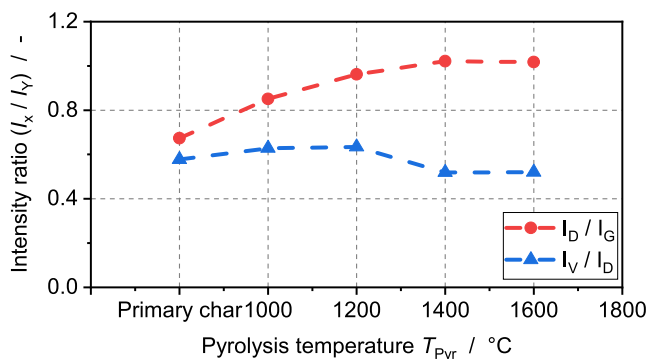
Fig. 9. Ratios of intensity maxima I_D/I_G and I_V/I_D as a function of pyrolysis temperature.

Fig. 10. CaO dispersion of secondary chars determined by TPR in a pTGA with CO_2 at 300 °C as a function of pyrolysis temperature.

the assumption that due to a low K/Si ratio, K may be deactivated by bonds to Si.

The average sizes of ash nanoparticles as a function of pyrolysis temperature is depicted in Fig. 14. For the evaluation of average particle size, between 650 and 900 particles were analyzed that were larger than 5 nm. The presence of an ash film was not taken into account for
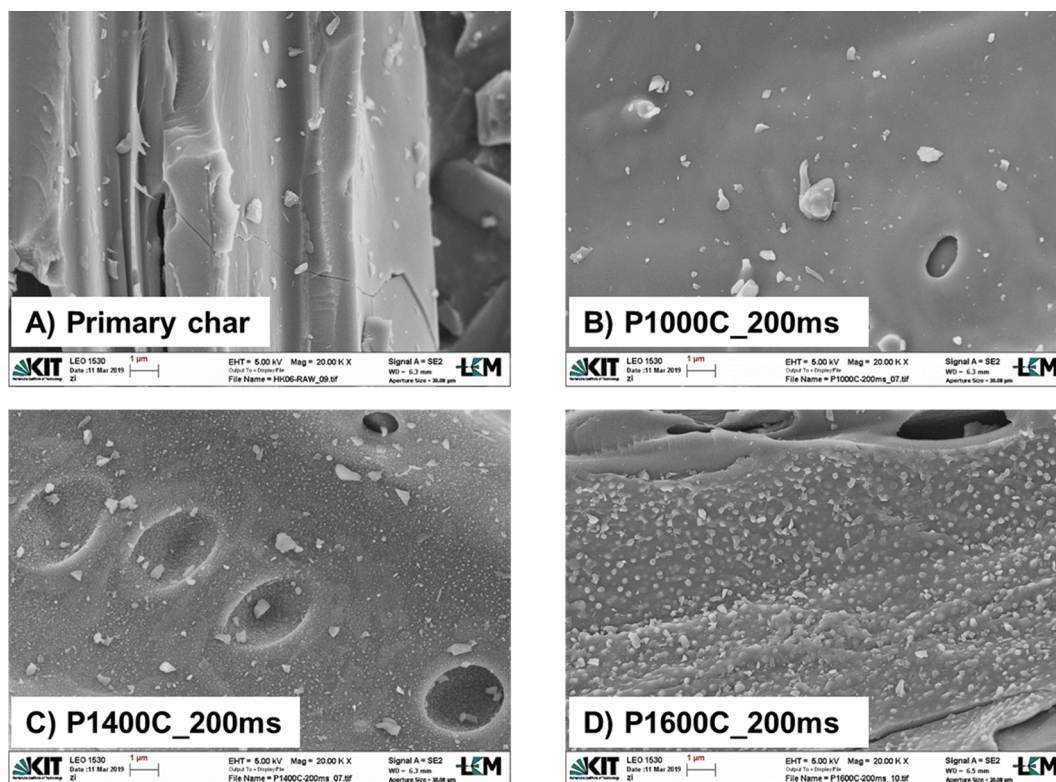
Fig. 11. SEM images of primary and secondary chars with $20,000\times$ magnification.
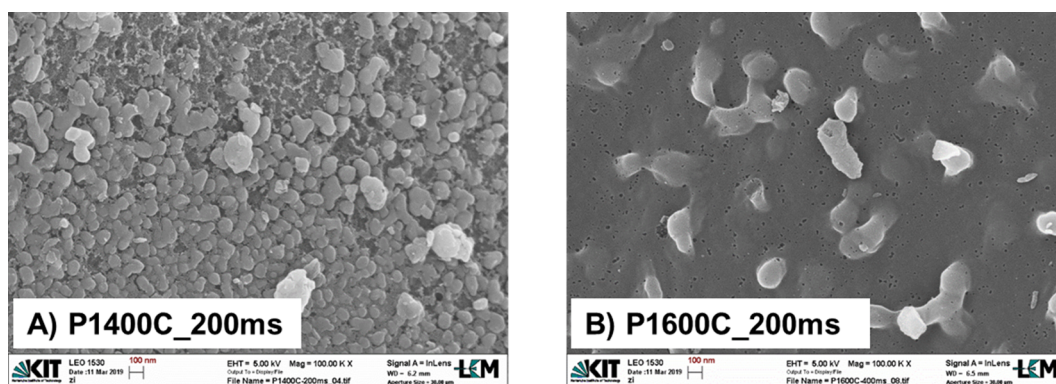
Fig. 12. SEM images of two secondary chars (P1400C_200ms and P1600C_200ms) with $100,000\times$ magnification.

this analysis. Average particle size slightly decreases from primary char to P1000C_200ms. Taking into account the large standard deviation of the analysis, it can be assumed that the ash nanoparticles on both samples may have almost the same size. Increasing the pyrolysis temperature from 1000 °C to 1400 °C leads to an increase in average particle size from approx. 10 nm to 18 nm. This is in good accordance with the Tammann temperature T_{Ta} = 1307 °C where mobility of CaO particles increases significantly. The largest ash particles were obtained

at 1600 °C with an average size of approx. 32 nm. Sintering of ash particles during pyrolysis was proven quantitatively by the particle size analysis as well as qualitatively observed via SEM images beforehand. However, increasing particle sizes do not necessarily have to involve a decrease in initial conversion rate R_0 of the gasification reaction with CO_2 as it can be seen for the char sample P1600C_200ms having the highest value for R_0 among the secondary chars.

To sum up, TEM-EDX images allowed for the identification of highly
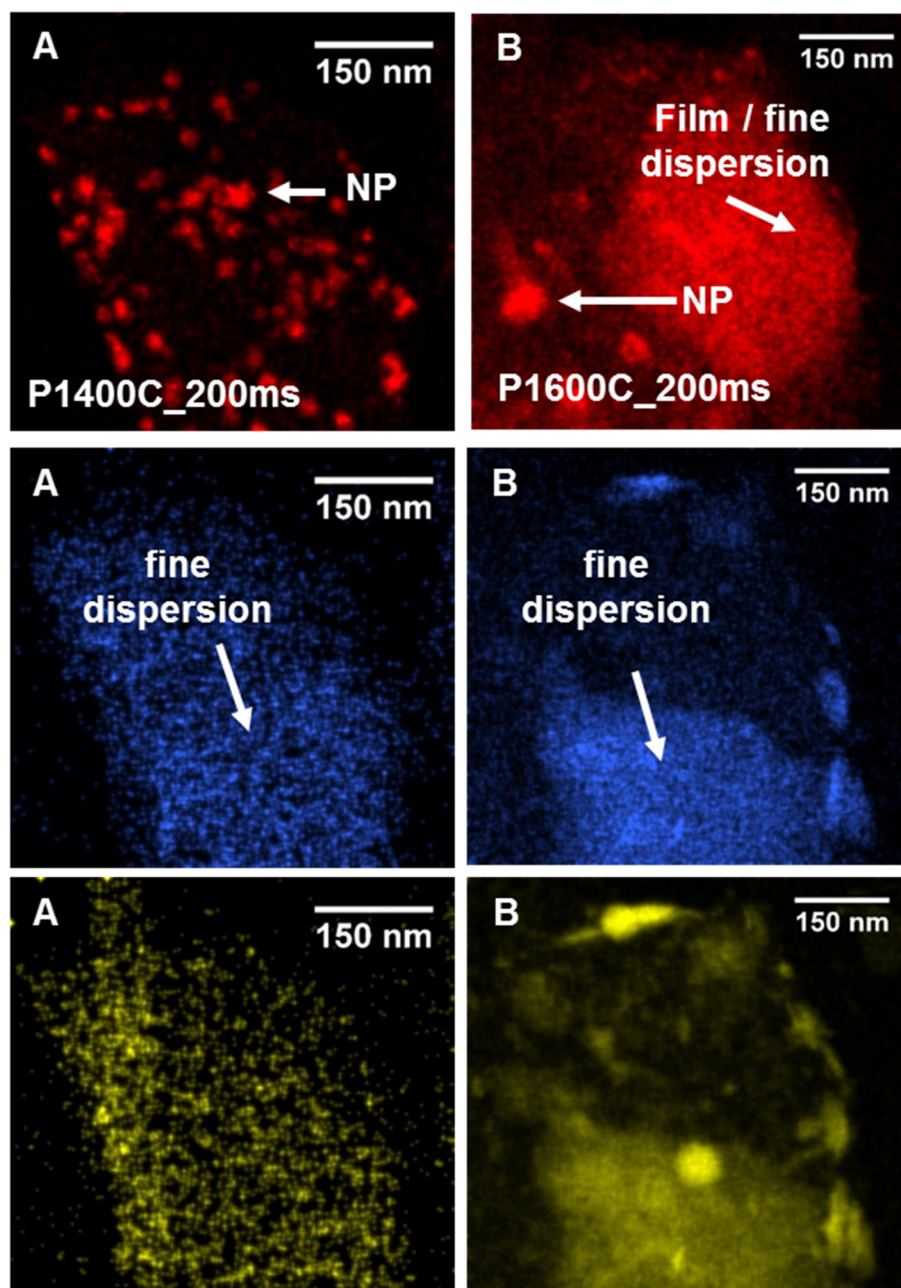
Fig. 13. TEM-EDX images of two secondary chars (P1400C_200ms (A) and P1600C_200ms (B)) visualizing the elements Ca (red), K (blue) and Si (yellow).

dispersed Ca compounds at a pyrolysis temperature of 1600 °C. Even the formation of a CaO film or thin layer can be deduced from SEM and TEM images. The high initial conversion rate R_0 of P1600C_200ms can be attributed to this thin layer of CaO. Due to the ash layer, a large contact area between both gas phase and catalyst as well as catalyst and carbon support is generated. The fact that a uniform thin layer of ash

particles on the carbon matrix catalyzes the gasification reaction with CO_2 supports the catalysis mechanisms described by Lobo & Carabineiro [30] and Cazorla-Amoros et al. [57] where the diffusion of a gaseous reactant through the catalyst layer plays a significant role.

Furthermore, the shape of the conversion curves and conversion rates depicted in Figs. 2 and 3 can be explained by the presence of
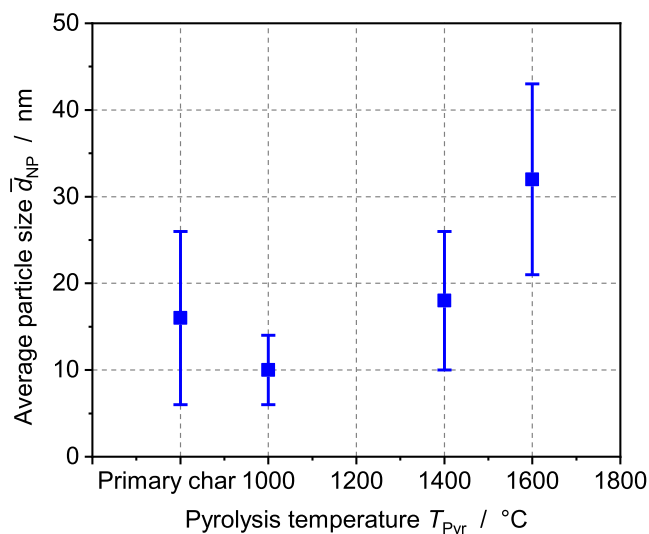
Fig. 14. Average sizes of ash nanoparticles as a function of pyrolysis temperature.
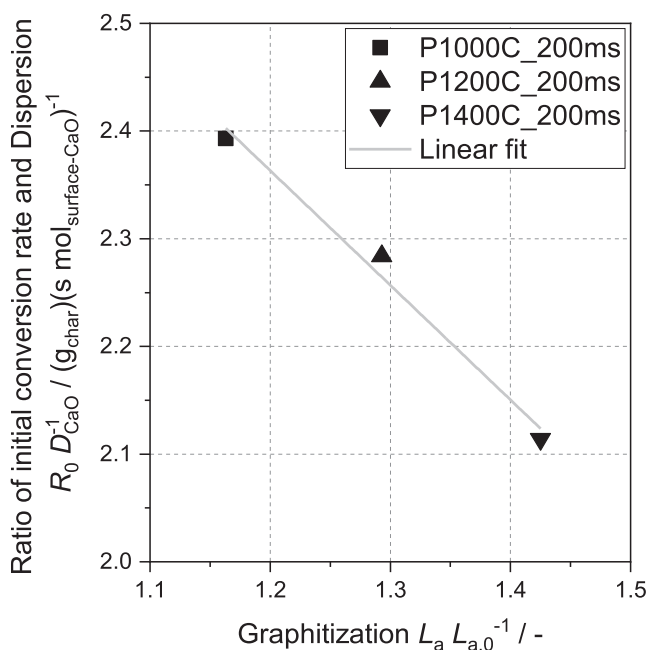
Fig. 15. The ratio of initial conversion rate R_0 and CaO dispersion D_{CaO} as a function of graphitization degree defined as $L_a L_{a,0}^{-1}$.

catalytic gasification induced by Ca. During calcium catalyzed gasification, the conversion rate decreases due to thermal deactivation processes of calcium particles which are mainly sintering [52]. This phenomenon can be observed for all samples except P1400C_200ms. From the constant conversion rate $\frac{dX}{dt}$ of P1400C_200ms can be deduced that the gasification of this sample is not or only to a small extent influenced by catalytic reactions. From both, long gasification time and linear shape of the conversion curve, it can be concluded that the uncatalyzed

carbon gasification is the dominant reaction for the sample P1400C_ms [44,70].

4.6. Influence of graphitization and ash dispersion on initial conversion rate R_0

In order to clarify the influence of graphitization on initial conversion rate R_0 of gasification with CO_2, the ratio of R_0 and CaO dispersion D_{CaO} is formed for pyrolysis temperatures between 1000 °C and 1400 °C. In Fig. 15, the ratio $R_0 D_{CaO}^{-1}$ is shown as a function of graphitization degree which is defined as the ratio of $L_a L_{a,0}^{-1}$. In this temperature range, which is later referred to as regime 1 (see Fig. 16), it can be seen that graphitization does have an impact on the initial conversion rate. The ratio $R_0 D_{CaO}^{-1}$ decreases linearly with increasing graphitization and consequently, with increasing pyrolysis temperature up to 1400 °C. Thus, when excluding the catalytic activity of CaO via formation of the ratio $R_0 D_{CaO}^{-1}$, increasing graphitization degree has a linear negative influence on char reactivity. However, both influences must be taken into account when investigating thermal deactivation due to thermal stress during high-temperature pyrolysis.

5. Summary and conclusions

Thermal deactivation of beech wood chars during secondary pyrolysis in a drop-tube reactor is presented. The effect of pyrolysis conditions on initial conversion rate R_0 during gasification, graphitization and ash dispersion was investigated. Gasification experiments for the determination of R_0 were conducted in a thermogravimetric analyzer using CO_2 at 750 °C. A linear decrease in the initial conversion rate between 1000 °C and 1400 °C was observed. However, a strong increase of R_0 at 1600 °C was encountered. Micropore surface area of the secondary chars showed no correlation with the initial conversion rate during gasification with CO_2. Graphitization of the carbon matrix was determined using X-ray diffraction and Raman spectroscopy suggesting the growth of aromatic clusters and graphite crystals for increasing pyrolysis temperatures. Furthermore, CaO dispersion was analyzed quantitatively and qualitatively using TPR at 300 °C as well as SEM/ TEM. CaO dispersion D_{CaO} decreases steadily between 1000 °C and 1400 °C whereas a strong increase can be observed at 1600 °C which is in good accordance with the development of the initial conversion rate R_0 as a function of pyrolysis temperature. SEM/TEM images indicate the formation of a thin CaO layer at 1600 °C which is presumably responsible for the strong increase in initial conversion rate R_0 at this temperature. When excluding the catalytic activity of CaO via formation of the ratio $R_0 D_{CaO}^{-1}$, increasing graphitization degree has a linear negative influence on char reactivity between 1000 °C and 1400 °C pyrolysis temperature.

Fig. 16 shows the most important experimental results of the present work summed up in one graph being the initial conversion rate R_0, CaO dispersion D_{CaO} and graphitization defined as $L_a L_{a,0}^{-1}$. In regime 1, the initial conversion rate and CaO dispersion decrease linearly with increasing pyrolysis temperature. Graphitization increases linearly with increasing pyrolysis temperature up to 1600 °C. However, the initial conversion rate R_0 of the char pyrolyzed at 1600 °C increases significantly despite showing the highest degree of graphitization. A strong correlation between initial conversion rate R_0 and CaO dispersion D_{CaO} is visible. D_{CaO} increases significantly for P1600C_200ms presumably due to the formation of a thin ash layer catalyzing the gasification reaction with CO_2.
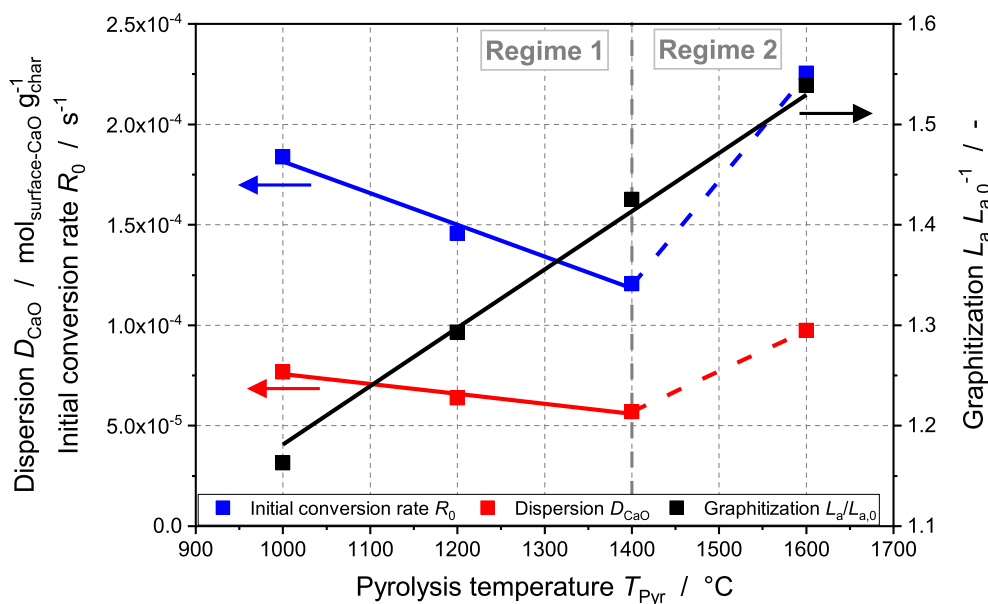
Fig. 16. Summary of the most important experimental results (CaO dispersion D_{CaO}, initial conversion rate R_0 and graphitization degree $L_a L_{a,0}^{-1}$) for the secondary chars.

In summary, secondary pyrolysis conditions have an influence on both graphitization of the carbon matrix and ash morphology which in turn affect the initial conversion rate R_0 during gasification with CO_2. Further research should investigate the formation of the observed catalyzing thin ash layer at high pyrolysis temperatures and its influence on the heterogeneous gasification reactions with CO_2 and H_2O.

6. Glossary

Symbol	Description	Unit
A	Specific surface area	$m^2\ g^{-1}$
B_a	FWHM of the (1 0 0)-Peak	cm^{-1}
B_c	FWHM of the (0 0 2)-Peak	cm^{-1}
D	Dispersion	$mol\ g^{-1}$
d	Distance between two lattice planes	m
$\bar{d}_{NP}$	Average particle size	m
$\frac{dX}{dt}$	Conversion rate	s^{-1}
I_D	Maximum intensity of the D-Peak	a.u.
I_G	Maximum intensity of the G-Peak	a.u.
I_V	Maximum intensity of the Valley-Peak	a.u.
K_a	Structural constant for Scherrer equation	-
K_c	Structural constant for Scherrer equation	-
l_{H1-3}	Length of the oven heating zones 1-3	m
L_a	Radial expansion of graphene layers	m
$L_{a,0}$	Radial expansion of graphene layers of the primary char	m
L_c	Stacking height of graphene layers	m
m	Mass	g
M_{CO_2}	Molar mass of CO_2	$g\ mol^{-1}$
n	Integer multiple	-
n_{CO_2}	Chemisorbed molar amount of CO_2	mol
R_0	Initial conversion rate	s^{-1}
R_m	Specific conversion rate	s^{-1}
R_X	Conversion rate	s^{-1}
t	Time	s
T	Temperature	°C
U	Accelerating voltage	V
X	Conversion	-
λ	Wave length	m
θ_a	Position of the (100)-Peak	°
θ_c	Position of the (002)-Peak	°

Subscripts	Description
CO_2	Carbon dioxide
surface-CaO	Superficial calcium oxide
Chem	Chemisorbed amount
Hü	Hüttig
melt	Melting point
MSA	Micropore surface area
Pyr	Pyrolysis
Stab	Stabilizing segment
Ta	Tamman

Abbreviations	Description
DR	Dubinin-Radushkevich
EDX	Energy-dispersive X-ray spectroscopy
EFG	Entrained-flow gasification
Eq.	Equation
Fig.	Figure
FWHM	Full-width at half maximum
HTSI	Heat treatment severity index
IAM-AWP	Institute for Applied Materials - Applied Materials Physics
ICP-OES	Inductively coupled plasma optical emission spectrometry
KIT	Karlsruhe Institute of Technology
LEM	Laboratory for Electron Microscopy
pTGA	Pressurized Thermogravimetric Analyzer
SEM	Scanning electron microscopy
TEM	Transmission electron microscopy
TPR	Temperature-programmed reaction
wt.	Weight
XRD	X-ray diffractometry

CRediT authorship contribution statement

Christoph Schneider: Conceptualization, Methodology, Validation, Investigation, Data curation, Writing - original draft, Visualization, Supervision, Project administration. **Stella Walker:** Methodology, Validation, Investigation, Data curation, Writing - review & editing. **Aekjuthon Phounglamcheik:** Methodology, Validation, Investigation, Data curation, Writing - review & editing. **Kentaro Umeki:** Resources, Writing - review & editing, Supervision. **Thomas Kolb:** Resources, Writing - review & editing, Supervision.

Declaration of Competing Interest

The authors declare that they have no known competing financial interests or personal relationships that could have appeared to influence the work reported in this paper.

Acknowledgements

Appendix A. Supplementary data

Supplementary data to this article can be found online at https://doi.org/10.1016/j.fuel.2020.118826.

References

[1] Dahmen N, Abeln J, Eberhard M, Kolb T, Leibold H, Sauer J, et al. The bioliq process for producing synthetic transportation fuels. WIREs Energy Environ 2017;6(3):e236https://doi.org/10.1002/wene.236.

[2] Higman C. State of the gasification industry-the updated worldwide gasification database. In: Gasification Technology Conference, Colorado Springs; 2013.

[3] Kolb T, Aigner M, Kneer R, Müller M, Weber R, Djordjevic N. Tackling the challenges in modelling entrained-flow gasification of low-grade feedstock. J Energy Inst 2016;89(4):485–503. https://doi.org/10.1016/j.joei.2015.07.007.

[4] Hurt R, Sun J-K, Lunden M. A Kinetic Model of Carbon Burnout in Pulverized Coal Combustion. Combust Flame 1998;113(1):181–97. https://doi.org/10.1016/S0010-2180(97)00240-X.

[5] Radovic LR, Steczko K, Walker PL, Jenkins RG. Combined effects of inorganic constituents and pyrolysis conditions on the gasification reactivity of coal chars. Fuel Process Technol 1985;10(3):311–26. https://doi.org/10.1016/0378-3820(85)90038-4.

[6] Senneca O, Salatino P, Masi S. Microstructural changes and loss of gasification reactivity of chars upon heat treatment. Fuel 1998;77(13):1483–93. https://doi.org/10.1016/S0016-2361(98)00056-8.

[7] Salatino P, Senneca O, Masi S. Assessment of thermodeactivation during gasification of a bituminous coal char. Energy Fuels 1999;13(6):1154–9. https://doi.org/10.1021/ef9900334.

[8] Russell NV, Gibbins JR, Williamson J. Structural ordering in high temperature coal chars and the effect on reactivity. Fuel 1999;78(7):803–7. https://doi.org/10.1016/S0016-2361(98)00210-5.

[9] Russell NV, Gibbins JR, Man CK, Williamson J. Coal char thermal deactivation under pulverized fuel combustion conditions. Energy Fuels 2000;14(4):883–8. https://doi.org/10.1021/ef990241w.

[10] Zanzi R, Sjöström K, Björnbom E. Rapid high-temperature pyrolysis of biomass in a free-fall reactor. Fuel 1996;75(5):545–50. https://doi.org/10.1016/0016-2361(95)00304-5.

[11] Zhang S-Y, Lu J-F, Zhang J-S, Yue G-X. Effect of Pyrolysis Intensity on the Reactivity of Coal Char. Energy Fuels 2008;22(5):3213–21. https://doi.org/10.1021/ef800245z.

[12] Di Blasi C. Combustion and gasification rates of lignocellulosic chars. Prog Energy Combust Sci 2009;35(2):121–40. https://doi.org/10.1016/j.pecs.2008.08.001.

[13] Ishimaru K, Hata T, Bronsveld P, Nishizawa T, Imamura Y. Characterization of sp2- and sp3-bonded carbon in wood charcoal. J Wood Sci 2007;53(5):442–8. https://doi.org/10.1007/s10086-007-0879-7.

[14] Lu L, Sahajwalla V, Kong C, Harris D. Quantitative X-ray diffraction analysis and its application to various coals. Carbon 2001;39(12):1821–33. https://doi.org/10.1016/S0008-6223(00)00318-3.

[15] Guo P, Saw WL, van Eyk PJ, Stechel EB, de Nys R, Ashman PJ, et al. Gasification reactivity and physicochemical properties of the chars from raw and torrefied wood, grape marc, and macroalgae. Energy Fuels 2017;31(3):2246–59. https://doi.org/10.1021/acs.energyfuels.6b02215.

[16] Oberlin A. Carbonization and graphitization. Carbon 1984;22(6):521–41. https://doi.org/10.1016/0008-6223(84)90086-1.

[17] Ferrari AC, Robertson J. Interpretation of Raman spectra of disordered and amorphous carbon. Phys. Rev. B 2000;61(20):14095–107. https://doi.org/10.1103/PhysRevB.61.14095.

[18] Ferrari AC, Robertson J. Raman spectroscopy of amorphous, nanostructured, diamond-like carbon, and nanodiamond. Philos Trans Ser A Math Phys Eng Sci 2004;362.

[19] Morin M, Pécate S, Hémati M, Kara Y. Pyrolysis of biomass in a batch fluidized bed reactor: Effect of the pyrolysis conditions and the nature of the biomass on the physicochemical properties and the reactivity of char. J Anal Appl Pyrol 2016;122:511–23. https://doi.org/10.1016/j.jaap.2016.10.002.

[20] Cetin E, Moghtaderi B, Gupta R, Wall TF. Influence of pyrolysis conditions on the structure and gasification reactivity of biomass chars. Fuel 2004;83(16):2139–50. https://doi.org/10.1016/j.fuel.2004.05.008.

[21] Septien S, Valin S, Peyrot M, Dupont C, Salvador S. Characterization of char and soot from millimetric wood particles pyrolysis in a drop tube reactor between 800°C and 1400°C. Fuel 2014;121:216–24. https://doi.org/10.1016/j.fuel.2013.12.026.

[22] Lu L, Kong C, Sahajwalla V, Harris D. Char structural ordering during pyrolysis and combustion and its influence on char reactivity. Fuel 2002;81(9):1215–25. https://doi.org/10.1016/S0016-2361(02)00035-2.

[23] Guerrero M, Ruiz MP, Millera Á, Alzueta MU, Bilbao R. Characterization of Biomass Chars Formed under Different Devolatilization Conditions: Differences between Rice Husk and Eucalyptus. Energy Fuels 2008;22(2):1275–84. https://doi.org/10.1021/ef7005589.

[24] Trubetskaya A, Jensen PA, Jensen AD, Steibel M, Spliethoff H, Glarborg P, et al. Comparison of high temperature chars of wheat straw and rice husk with respect to chemistry, morphology and reactivity. Biomass Bioenergy 2016;86:76–87. https://doi.org/10.1016/j.biombioe.2016.01.017.

[25] Guizani C, Jeguirim M, Valin S, Peyrot M, Salvador S. The Heat Treatment Severity Index: A new metric correlated to the properties of biochars obtained from entrained flow pyrolysis of biomass. Fuel 2019;244:61–8. https://doi.org/10.1016/j.fuel.2019.01.170.

[26] Senneca O, Apicella B, Russo C, Cerciello F, Salatino P, Heuer S, et al. Pyrolysis and thermal annealing of coal and biomass in CO2 -rich atmospheres. Energy Fuels 2018;32(10):10701–8. https://doi.org/10.1021/acs.energyfuels.8b02417.

[27] Mahinpey N, Gomez A. Review of gasification fundamentals and new findings: Reactors, feedstock, and kinetic studies. Chem Eng Sci 2016;148:14–31. https://doi.org/10.1016/j.ces.2016.03.037.

[28] Irfan MF, Usman MR, Kusakabe K. Coal gasification in CO2 atmosphere and its kinetics since 1948: A brief review. Energy 2011;36(1):12–40. https://doi.org/10.1016/j.energy.2010.10.034.

[29] Lobo LS. Intrinsic kinetics in carbon gasification: Understanding linearity, "nano-worms" and alloy catalysts. Appl Catal B 2014;148–149:136–43. https://doi.org/10.1016/j.apcatb.2013.09.048.

[30] Lobo LS, Carabineiro SAC. Kinetics and mechanism of catalytic carbon gasification. Fuel 2016;183:457–69. https://doi.org/10.1016/j.fuel.2016.06.115.

[31] Wood BJ, Sancier KM. The Mechanism of the Catalytic Gasification of Coal Char: A Critical Review. Catal Rev 2006;26(2):233–79. https://doi.org/10.1080/01614948408078065.

[32] Huang Y, Yin X, Wu C, Wang C, Xie J, Zhou Z, et al. Effects of metal catalysts on CO2 gasification reactivity of biomass char. Biotechnol Adv 2009;27(5):568–72. https://doi.org/10.1016/j.biotechadv.2009.04.013.

[33] Baker RTK, Chludzinski JJ. Catalytic gasification of graphite by calcium and nickel-calcium. Carbon 1985;23(6):635–44. https://doi.org/10.1016/0008-6223(85)90223-4.

[34] Bouraoui Z, Dupont C, Jeguirim M, Limousy L, Gadiou R. CO2 gasification of woody biomass chars: The influence of K and Si on char reactivity. C R Chim 2016;19(4):457–65. https://doi.org/10.1016/j.crci.2015.08.012.

[35] Dupont C, Jacob S, Marrakchy KO, Hognon C, Grateau M, Labalette F, et al. How inorganic elements of biomass influence char steam gasification kinetics. Energy 2016;109:430–5. https://doi.org/10.1016/j.energy.2016.04.094.

[36] Kapteijn F, Abbel G, Moulijn JA. CO2 gasification of carbon catalysed by alkali metals: Reactivity and mechanism. Fuel 1984;63(8):1036–42. https://doi.org/10.1016/0016-2361(84)90184-4.

[37] Kirtania K, Axelsson J, Matsakas L, Christakopoulos P, Umeki K, Furusjö E. Kinetic study of catalytic gasification of wood char impregnated with different alkali salts. Energy 2017;118:1055–65. https://doi.org/10.1016/j.energy.2016.10.134.

[38] Kopyscinski J, Habibi R, Mims CA, Hill JM. K2CO3-Catalyzed CO2 Gasification of Ash-Free Coal: Kinetic Study. Energy Fuels 2013;27(8):4875–83. https://doi.org/10.1021/ef400552q.

[39] Aho A, DeMartini N, Pranovich A, Krogell J, Kumar N, Eränen K, et al. Pyrolysis of pine and gasification of pine chars – Influence of organically bound metals. Bioresour Technol 2013;128:22–9. https://doi.org/10.1016/j.biortech.2012.10.093.

[40] Duman G, Uddin MA, Yanik J. The effect of char properties on gasification reactivity. Fuel Process Technol 2014;118:75–81. https://doi.org/10.1016/j.fuproc.2013.08.006.

[41] Kramb J, Gómez-Barea A, DeMartini N, Romar H, Doddapaneni TRKC, Konttinen J. The effects of calcium and potassium on CO2 gasification of birch wood in a fluidized bed. Fuel 2017;196:398–407. https://doi.org/10.1016/j.fuel.2017.01.101.

[42] Lahijani P, Zainal ZA, Mohamed AR, Mohammadi M. CO2 gasification reactivity of biomass char: Catalytic influence of alkali, alkaline earth and transition metal salts. Bioresour Technol 2013;144:288–95. https://doi.org/10.1016/j.biortech.2013.06.059.

[43] Mitsuoka K, Hayashi S, Amano H, Kayahara K, Sasaoka E, Uddin MA. Gasification of woody biomass char with CO2: The catalytic effects of K and Ca species on char gasification reactivity. Fuel Process Technol 2011;92(1):26–31. https://doi.org/10.1016/j.fuproc.2010.08.015.

[44] Struis RPWJ, Cv S, Stucki S, Prins R. Gasification reactivity of charcoal with CO2.

Part II: Metal catalysis as a function of conversion. Chem Eng Sci 2002;57(17):3593–602. https://doi.org/10.1016/S0009-2509(02)00255-5.

[45] Zhang Y, Ashizawa M, Kajitani S, Miura K. Proposal of a semi-empirical kinetic model to reconcile with gasification reactivity profiles of biomass chars. Fuel 2008;87(4):475–81. https://doi.org/10.1016/j.fuel.2007.04.026.

[46] Zhang Y, Hara S, Kajitani S, Ashizawa M. Modeling of catalytic gasification kinetics of coal char and carbon. Fuel 2010;89(1):152–7. https://doi.org/10.1016/j.fuel.2009.06.004.

[47] Kapteijn F, Porre H, Moulijn JA. CO2 gasification of activated carbon catalyzed by earth alkaline elements. AIChE J 1986;32(4):691–5. https://doi.org/10.1002/aic.690320421.

[48] Marquez-Montesinos F, CorderoRodríguez-Mirasol J, Rodríguez JJ. T. CO2 and steam gasification of a grapefruit skin char. Fuel 2002;81(4):423–9. https://doi.org/10.1016/S0016-2361(01)00174-0.

[49] Kuznetsov PN, Kolesnikova SM, Kuznetsova LI. Steam gasification of different brown coals catalysed by the naturally occurring calcium species. Int J Clean Coal Energy 2013;2(01):1.

[50] Hognon C, Dupont C, Grateau M, Delrue F. Comparison of steam gasification reactivity of algal and lignocellulosic biomass: Influence of inorganic elements. Bioresour Technol 2014;164:347–53. https://doi.org/10.1016/j.biortech.2014.04.111.

[51] Argyle M, Bartholomew C. Heterogeneous Catalyst Deactivation and Regeneration: A Review. Catalysts 2015;5(1):145–269. https://doi.org/10.3390/catal5010145.

[52] Cazorla-Amoros D, Linares-Solano A, Salinas-Martinez de Lecea C, Yamashita H, Kyotani T, Tomita A, et al. XAFS and thermogravimetry study of the sintering of calcium supported on carbon. Energy Fuels 1993;7(1):139–45.

[53] Vannice MA, Joyce WH. Kinetics of catalytic reactions. New York (NY): Springer; 2005.

[54] Kuznetsov PN, Kuznetsova LI, Mikhlin YL. Chemical forms and distribution of naturally occurring calcium in brown coal chars. Fuel 2015;162:207–10. https://doi.org/10.1016/j.fuel.2015.09.015.

[55] Cazorla-Amoros D, Linares-Solano A, Salinas-Martinez de Lecea C, Joly JP. A temperature-programmed reaction study of calcium-catalyzed carbon gasification. Energy Fuels 1992;6(3):287–93. https://doi.org/10.1021/ef00033a008.

[56] Zhang Y, Ashizawa M, Kajitani S. Calcium loading during the dewatering of wet biomass in kerosene and catalytic activity for subsequent char gasification. Fuel 2008;87(13):3024–30. https://doi.org/10.1016/j.fuel.2008.03.009.

[57] Cazorla-Amorós D, Linares-Solano A, Lecea CS-Md, Joly JP. Calcium-carbon interaction study: Its importance in the carbon-gas reactions. Carbon 1991;29(3):361–9. https://doi.org/10.1016/0008-6223(91)90205-W.

[58] Linares-Solano A, Almela-Alarcón M, Lecea CS-Md. CO2 chemisorption to characterize calcium catalysts in carbon gasification reactions. J Catal 1990;125(2):401–10. https://doi.org/10.1016/0021-9517(90)90313-9.

[59] Cazorla-Amoros D, Linares-Solano A, Salinas-Martinez de Lecea C, Nomura M, Yamashita H, Tomita A. Local structure of calcium species dispersed on carbon:

Influence of the metal loading procedure and its evolution during pyrolysis. Energy Fuels 1993;7(5):625–31.

[60] Guizani C, Jeguirim M, Valin S, Limousy L, Salvador S. Biomass chars: the effects of pyrolysis conditions on their morphology, structure, chemical properties and reactivity. Energies 2017;10(6):796. https://doi.org/10.3390/en10060796.

[61] Strandberg A, Holmgren P, Wagner DR, Molinder R, Wiinikka H, Umeki K, et al. Effects of pyrolysis conditions and ash formation on gasification rates of biomass char. Energy Fuels 2017;31(6):6507–14. https://doi.org/10.1021/acs.energyfuels.7b00688.

[62] Stoesser P, Schneider C, Kreitzberg T, Kneer R, Kolb T. On the influence of different experimental systems on measured heterogeneous gasification kinetics. Appl Energy 2018;211:582–9. https://doi.org/10.1016/j.apenergy.2017.11.037.

[63] Stoesser P. Investigation of solid phase processes during the conversion of biogenic slurry in entrained flow gasifiers. Munich: Dr. Hut; 2020.

[64] Feng B, Bhatia SK, Barry JC. Variation of the crystalline structure of coal char during gasification. Energy Fuels 2003;17(3):744–54. https://doi.org/10.1021/ef0202541.

[65] Saikia BK, Boruah RK, Gogoi PK. A X-ray diffraction analysis on graphene layers of Assam coal. J Chem Sci 2009;121(1):103–6.

[66] Tuinstra F, Koenig JL. Raman spectrum of graphite. J Chem Phys 1970;53(3):1126–30. https://doi.org/10.1063/1.1674108.

[67] Rhim Y-R, Zhang D, Fairbrother DH, Wepasnick KA, Livi KJ, Bodnar RJ, et al. Changes in electrical and microstructural properties of microcrystalline cellulose as function of carbonization temperature. Carbon 2010;48(4):1012–24. https://doi.org/10.1016/j.carbon.2009.11.020.

[68] Haynes WM. CRC Handbook of Chemistry and Physics, 92nd Edition. 92nd ed. Hoboken: CRC Press; 2011.

[69] Dupont C, Nocquet T, Costa JAD, Verne-Tournon C. Kinetic modelling of steam gasification of various woody biomass chars: Influence of inorganic elements. Bioresour Technol 2011;102(20):9743–8. https://doi.org/10.1016/j.biortech.2011.07.016.

[70] Kramb J, DeMartini N, Perander M, Moilanen A, Konttinen J. Modeling of the catalytic effects of potassium and calcium on spruce wood gasification in CO2. Fuel Process Technol 2016;148:50–9. https://doi.org/10.1016/j.fuproc.2016.01.031.

[71] Tremel A, Spliethoff H. Gasification kinetics during entrained flow gasification – Part I; Devolatilisation and char deactivation. Fuel 2013;103:663–71. https://doi.org/10.1016/j.fuel.2012.09.014.

[72] Liu H, Luo C, Kato S, Uemiya S, Kaneko M, Kojima T. Kinetics of CO2/Char gasification at elevated temperatures: Part I: Experimental results. Fuel Process Technol 2006;87(9):775–81. https://doi.org/10.1016/j.fuproc.2006.02.006.

[73] Franklin RE. The structure of graphitic carbons. Acta Cryst 1951;4(3):253–61. https://doi.org/10.1107/S0365110X51000842.

[74] Di Blasi C. Modeling chemical and physical processes of wood and biomass pyrolysis. Prog Energy Combust Sci 2008;34(1):47–90. https://doi.org/10.1016/j.pecs.2006.12.001.